Chemistry Europe
European Chemical Societies Publishing

WILEY VCH

Excellence in Chemistry Research

Announcing our new flagship journal

- Gold Open Access
- Publishing charges waived
- Preprints welcome
- Edited by active scientists

Meet the Editors of *ChemistryEurope*

Luisa De Cola
Università degli Studi di Milano Statale, Italy

Ive Hermans
University of Wisconsin-Madison, USA

Ken Tanaka
Tokyo Institute of Technology, Japan

Chemistry–A European Journal
Research Article
doi.org/10.1002/chem.202300821
Chemistry Europe
European Chemical Societies Publishing
www.chemeurj.org

Phosphate-functionalized Zirconium Metal–Organic Frameworks for Enhancing Lithium–Sulfur Battery Cycling

Bingqian Liu,[a] Avery E. Baumann,[a, b] Megan M. Butala,[b, c] and V. Sara Thoi*[a, d]

Abstract: Lithium–sulfur batteries are promising candidates for next-generation energy storage devices due to their outstanding theoretical energy density. However, they suffer from low sulfur utilization and poor cyclability, greatly limiting their practical implementation. Herein, we adopted a phosphate-functionalized zirconium metal–organic framework (Zr-MOF) as a sulfur host. With their porous structure, remarkable electrochemical stability, and synthetic versatility, Zr-MOFs present great potential in preventing soluble polysulfides from leaching. Phosphate groups were introduced to the framework post-synthetically since they have shown a strong affinity towards lithium polysulfides and an ability to facilitate Li ion transport. The successful incorporation of phosphate in MOF-808 was demonstrated by a series of techniques including infrared spectroscopy, solid-state nuclear magnetic resonance spectroscopy, and X-ray pair distribution function analysis. When employed in batteries, phosphate-functionalized Zr-MOF (MOF-808-PO4) exhibits significantly enhanced sulfur utilization and ion diffusion compared to the parent framework, leading to higher capacity and rate capability. The improved capacity retention and inhibited self-discharge rate also demonstrate effective polysulfide encapsulation utilizing MOF-808-PO4. Furthermore, we explored their potential towards high-density batteries by examining the cycling performance at various sulfur loadings. Our approach to correlate structure with function using hybrid inorganic–organic materials offers new chemical design strategies for advancing battery materials.

Introduction

Although lithium ion batteries (LIB) have been widely used in almost every aspect of the modern society, the conventional cathode and anode materials based on lithium insertion are approaching their theoretical capacity, limiting their continued implementation in all-electric vehicles and grid energy storage devices.[1] With their exceptional theoretical gravimetric energy density (2,572 Wh kg^{-1}) and the high earth abundance of sulfur, lithium–sulfur (Li–S) batteries are promising candidates for next-generation energy storage devices.[2] However, Li–S batteries are faced with several technical challenges that impede their practical applications. The insulating nature of elemental sulfur greatly restricts the effective utilization of active materials and inhibits high sulfur loading for achieving energy and power density necessary for commercialization. Moreover, the well-known shuttle effect, caused by dissolution of soluble polysulfides into the electrolyte, leads to rapid capacity decay and high self-discharge rate.[3,4]

Extensive efforts have been undertaken to address the polysulfide leaching phenomenon. Adopting a host material at the cathode to encapsulate soluble polysulfides is one promising approach. Compared to commonly used polysulfide host materials such as porous carbon materials,[5,6] metal oxides,[7,8] metal sulfides,[9] and polymers,[10,11] metal–organic frameworks (MOFs) present unique advantages owing to their highly tunable physical and chemical properties. MOFs are a class of hybrid organic-inorganic porous crystalline materials composed of metal nodes and organic linkers. Rational selection and combination of nodes and linkers can be used to tailor properties, such as porosity, particle morphology, polarity and conductivity, for desired applications. Additionally, their porous nature and easily accessible defective sites permit host–guest interactions and facile functionalization.[12,13] The tunability over their structural and chemical properties enables polysulfide confinement via both physical encapsulation and chemical anchoring. Furthermore, there have been extensive efforts aimed at enhancing charge transport in MOFs by tuning electronic, ionic, and structural properties of the nodes and linkers.[14–18] Thus, MOFs with various composition, functionaliza-

[a] Dr. B. Liu, Dr. A. E. Baumann, Prof. Dr. V. S. Thoi
Department of Chemistry
Johns Hopkins University
Baltimore, MD 21218 (United States)
[b] Dr. A. E. Baumann, Prof. Dr. M. M. Butala
National Institute of Standards and Technology
Gaithersburg, MD 20899 (USA)
[c] Prof. Dr. M. M. Butala
Department of Materials Science and Engineering
University of Florida
Gainesville, FL 32611 (USA)
[d] Prof. Dr. V. S. Thoi
Department of Materials Science and Engineering
Johns Hopkins University
Baltimore, MD 21218 (United States)

Supporting information for this article is available on the WWW under https://doi.org/10.1002/chem.202300821

tion and pore structures have been used in Li–S cathodes (Table S1) to mitigate polysulfide leaching and promote charge conduction.[19–26]

Due to their strong affinity with lithium polysulfides and ability to promote Li ion transport, phosphate-based separators[27–29] and sulfur hosts[30,31] have been previously utilized in Li–S batteries to improve their cycling performance. Phosphates are also known flame retardants and have been used as electrolyte additives to construct safer batteries.[32,33] In addition, we have previously shown that thiophosphate functionalization of Zr-MOFs significantly improved sulfur utilization and rate capability.[34–36] However, electrode fabrication of these materials were challenged by their air sensitivity. Inspired by these studies, we incorporated air-stable phosphate groups into a three-dimensional porous MOF matrix to mitigate lithium polysulfide dissolution and accelerate redox processes (Scheme 1). The successful incorporation of phosphate was demonstrated by a series of spectroscopic techniques. Employing phosphate-functionalized MOF-808 (MOF-808-PO4) as the sulfur host, MOF-808-PO4/S composite cathodes exhibit reduced self-discharge rate, enhanced sulfur utilization, and accelerated charge diffusion compared to MOF-808/S cathodes. As a result, MOF-808-PO4/S cathodes achieve high capacity retention and rate performance. Moreover, we investigated the electrochemical performance at various sulfur loadings (as high as 3.3 mg cm^{-2}) to evaluate their potentials in high loading batteries.

Results and Discussion

Materials synthesis and characterization

We first explored previous methodologies for binding phosphate groups to Zr nodes.[37–39] MOF-808, a well-known Zr-based MOF comprised of benzene-1,3,5-tricarboxylic acid, was selected due to its outstanding electrochemical stability and synthetic tunability.[40] Each secondary building unit in MOF-808 is 6-coordinated, leaving six open sites bound by monotopic ligands (e.g., formate and H_2O/OH^-) to balance the charge. These monotopic ligand-bound sites are labile, making MOF-808 facile to undergo defect introduction and ligand exchange.[41] Adopting a slightly modified solvent-assisted ligand incorporation procedure,[39,42] MOF-808-PO4 was synthesized by soaking MOF-808 in Li_3PO_4/formic acid aqueous solution (Scheme 2). Formic acid was added to the solution to fully dissolve Li_3PO_4 in water.

The structural integrity of MOF-808 after ligand exchange was confirmed by powder X-ray diffraction (PXRD). As shown in Figure S1, the powder X-ray diffraction (PXRD) pattern of MOF-808-PO4 matches well with that of the parent MOF, with only minor crystallinity loss. Fourier transform infrared (FTIR) spectroscopy of MOF-808-PO4 (Figure 1a) exhibit a broad peak at 1037 cm^{-1}, corresponding to the asymmetric stretching vibration in the PO_4^{3-} group. The bands around 565 cm^{-1} and 610 cm^{-1} are due to bending vibrations of PO_4^{3-} group.[43] Nitrogen adsorption isotherms measured at 77 K (Figure S2) illustrate the incorporation of phosphate groups lead to reduced gas uptake and blocked pore volume.

Elemental analysis by inductively coupled plasma optical emission spectroscopy (ICP-OES) was used to quantify the Zr and P content in MOF-808-PO4. The results show a P/Zr mass ratio of 0.186, suggesting an average of 3.3 equiv. phosphate per Zr_6 node was incorporated into the framework (6 equiv. sites per node are theoretically available for incorporation). The successful incorporation of phosphate groups was also confirmed by phosphorus nuclear magnetic resonance (^{31}P NMR) spectroscopy. MOF-808-PO4 was digested in 1 M NaOH/D_2O overnight for liquid-phase ^{31}P NMR spectroscopy. A single peak with a chemical shift of 5.58 ppm was observed, demonstrating the presence of PO_4^{3-} group (Figure S3). Solid-state ^{31}P NMR spectroscopy was performed to further identify the local

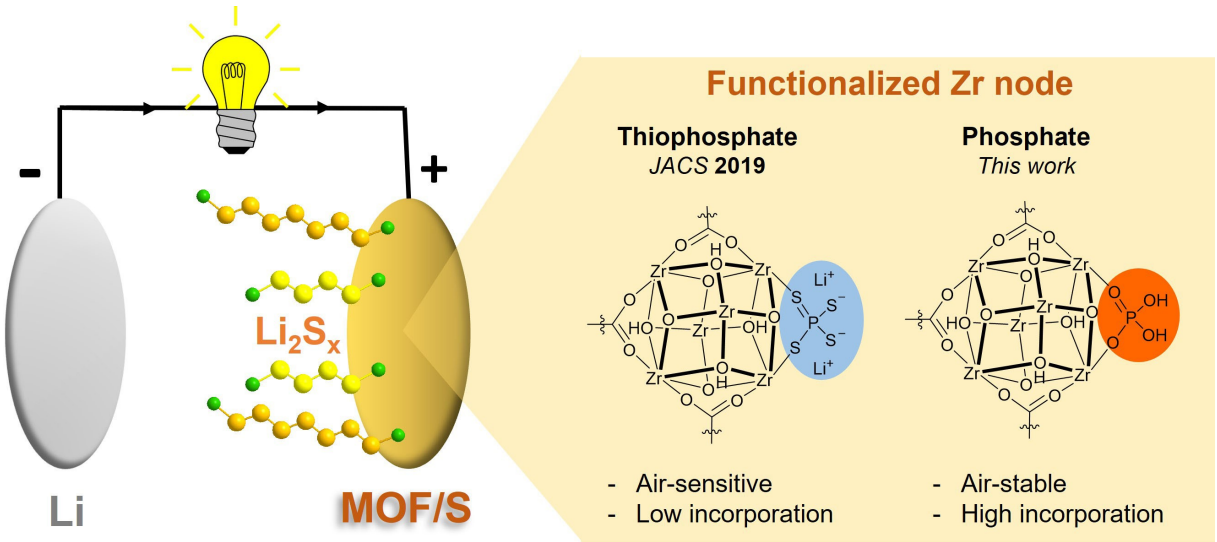

Scheme 1. Comparison of thiophosphate[34] and phosphate-functionalized Zr-MOFs as sulfur hosts for Li–S battery.

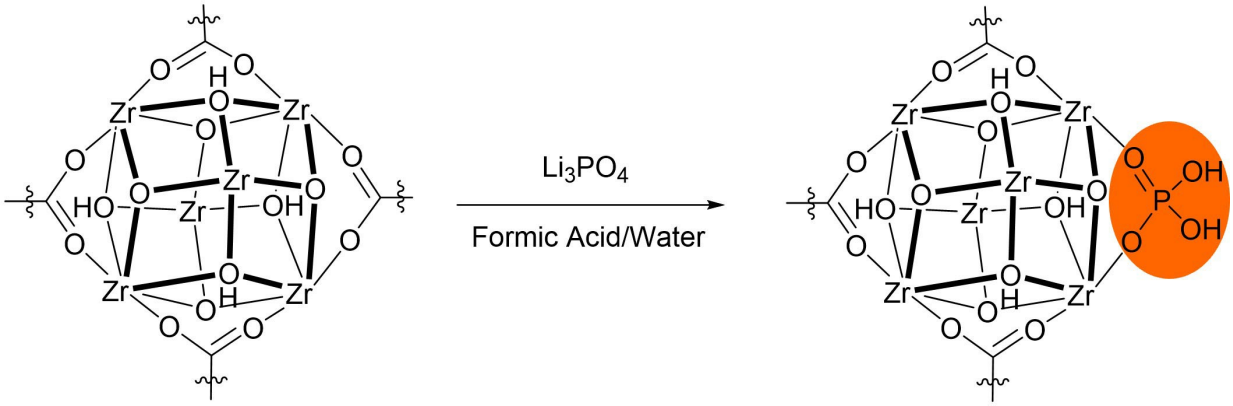

Scheme 2. Phosphate functionalization via solvent-assisted ligand incorporation treatment. Phosphate groups are incorporated to the hexanuclear node post-synthetically by replacing a formate ligand or H_2O/OH^- terminal groups. Only 1/3 of the carboxylate ligands are shown for clarity.

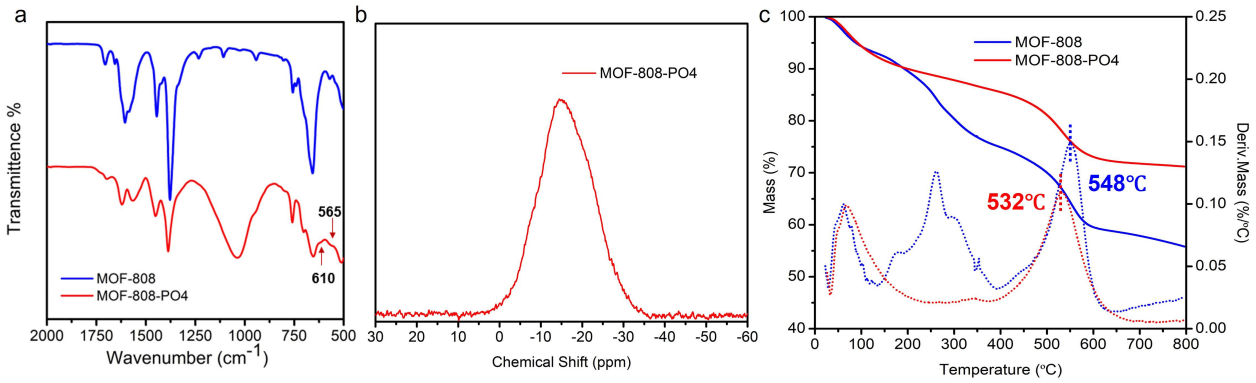

Figure 1. a) IR spectra of MOF-808-PO4 and MOF-808, b) MAS ^{31}P NMR of MOF-808-PO4, and c) TGA curves of MOF-808-PO4 and MOF-808.

environment of the phosphate in the framework. ^{31}P NMR spectrum of MOF-808-PO4 (Figure 1b) shows a single peak centered at −15.6 ppm, which is tentatively assigned to a Zr-bound PO_4^{3-} group.[44] The upfield shift in the phosphorus resonance compared to Li_3PO_4 reference at 9.47 ppm (Figure S4) and unbound phosphate at ≈−0.3 ppm[39] confirm the different chemical environment of phosphates in the framework, further suggesting the formation of a Zr-phosphate bond. The thermal stability of MOFs before and after functionalization (Figure 1c) was characterized by thermogravimetric analysis (TGA). The introduction of phosphates leads to slightly lower decomposition temperature (532 °C) compared to pristine MOF-808 (548 °C), suggesting a small decrease in thermal stability. The mass loss events at < 200 °C and 200 °C to 300 °C result from residual solvent and node-bound formate in MOF-808, respectively.[45] We note that there is less mass loss in the range of 200 °C to 300 °C for MOF-808-PO4 compared to parent MOF, suggesting the formate ligands bound to the open sites have been successfully replaced with phosphate group.

The structure of the Zr node before and after introduction of the phosphate groups was evaluated using X-ray pair distribution function (PDF) analysis on MOF-808 and MOF-808-PO4 samples (Figure 2 and Figure S5). The local atom pair correlations, represented by the function G(r), of each sample and the difference curve are plotted in Figure 2a. The peak positions represent interatomic radial distances and peak area is related to the relative abundance of an atom-atom correlation length weighted by atomic number (for X-rays).The most pronounced differences between the two samples occur at radial distances 2.2 Å and 3.5 Å, which have been established as the Zr–O and Zr–Zr pairs in the Zr_6 cluster both in our model (Figure 2b) and in other reports.[46–48] Changes to the nodal peaks support that the phosphate is bound to the Zr node, which we have previously noted in another study,[34] and is consistent with the results of solid-state ^{31}P NMR and TGA. Another difference at ≈1.5 Å in MOF-808-PO4 is attributed to the P–O pair and presents along with more subtle peaks at higher distances, in agreement with a node-bound phosphate species.[49] Since our model only introduces one phosphate moiety, the nodal pairs (Zr–Zr and Zr–O) are more highly weighted in their calculated G(r) when, in reality, an average of 3.3 phosphate molecules are expected to bind per node based on ICP-OES results. We highlight these regions in Figure 2b to guide the eye to areas of interest in the difference curve.

The absorptivity towards polysulfide species was evaluated by soaking MOF powders in a lithium polysulfide solution for

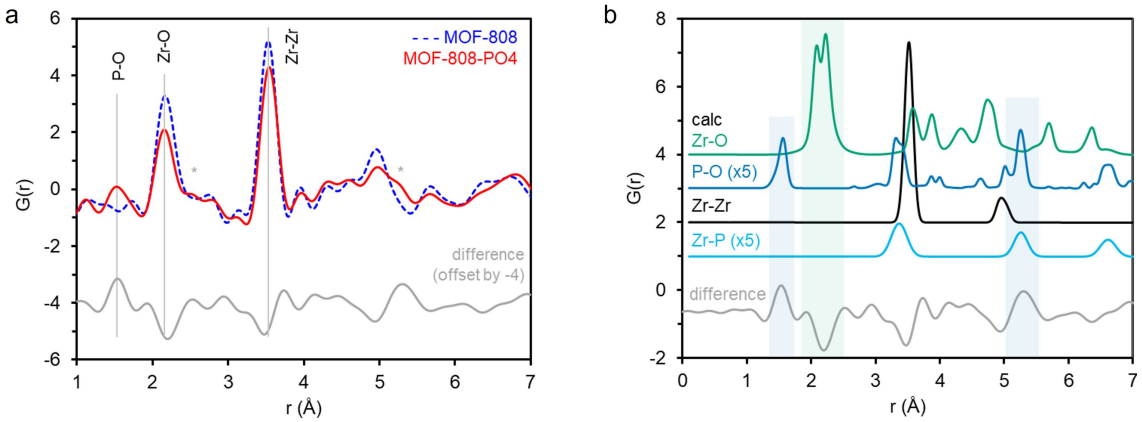

Figure 2. a) Experimental X-ray pair distribution functions showing the pairwise atom-atom correlations in MOF-808 (dashed) and MOF-808-PO4 (solid). The difference curve at the bottom of the graph was obtained by subtracting the MOF-808 G(r) from MOF-808-PO4. b) Calculated atom-atom correlations obtained from optimized structures by element compared to the experimental difference function. The peaks indicated in (a) are highlighted in (b) for visual comparison of the measured and calculated curves.

24 h. After soaking, an obvious color change of the solution from deep orange to clear was observed (Figure S6). UV-vis spectra of polysulfide solution with and without MOF added are shown in Figure S7. The obvious decrease in peak absorbances at 420 nm (S_4^{2-}) and 618 nm ($S_3^{\bullet-}$ radical) in the supernatant validates that the porous structure of MOF-808 and MOF-808-PO4 are capable of uptaking lithium polysulfides from solution, with a slight absorption enhancement by MOF-808-PO4.[50]

Li-S cycling performance and analysis

The electrochemical performance of MOF-808-PO4 as sulfur host was investigated in Li–S cells (electrolyte/sulfur ratio = 60 μL mg^{-1} S). Cyclic voltammetry (CV) scan-rate dependence experiments (Figure 3a, Figure S8) were performed on cells composed of MOF/S composite cathodes, cycling between 1.6 V and 2.9 V (vs. Li/Li^+). Both MOF-808/S and MOF-808-PO4/S cells exhibit one broad oxidation peak at ≈2.5 V and two reduction events at ≈2.3 V and ≈2.0 V, corresponding to the reduction from sulfur to polysulfide and polysulfide to Li_2S, respectively. They also show a good linear fit when sulfur-normalized peak currents (in A per g of sulfur, A g^{-1} S) are plotted against the square root of the scan rate, confirming the sulfur and polysulfide reduction reactions are diffusion controlled (Figure 3b–c). The slope of the linear fit is a proxy for the diffusion coefficient of electroactive species according to Randles–Sevcik equation.[51] Compared to MOF-808/S cathode, the larger slopes of MOF-808-PO4/S cathode in both reduction stages suggest phosphate incorporation effectively promote ion diffusion during cycling. Additionally, the increased peak currents in MOF-808-PO4/S cells, especially at faster scan rates, further demonstrate MOF-808-PO4 additives are able to promote active material utilization.

High self-discharge rate due to the polysulfide shuttle effect is a major drawback, leading to poor shelf life and capacity decay.[52] The decline in open circuit potential (OCP) over an 8-hour rest time was monitored on cells with different MOF hosts

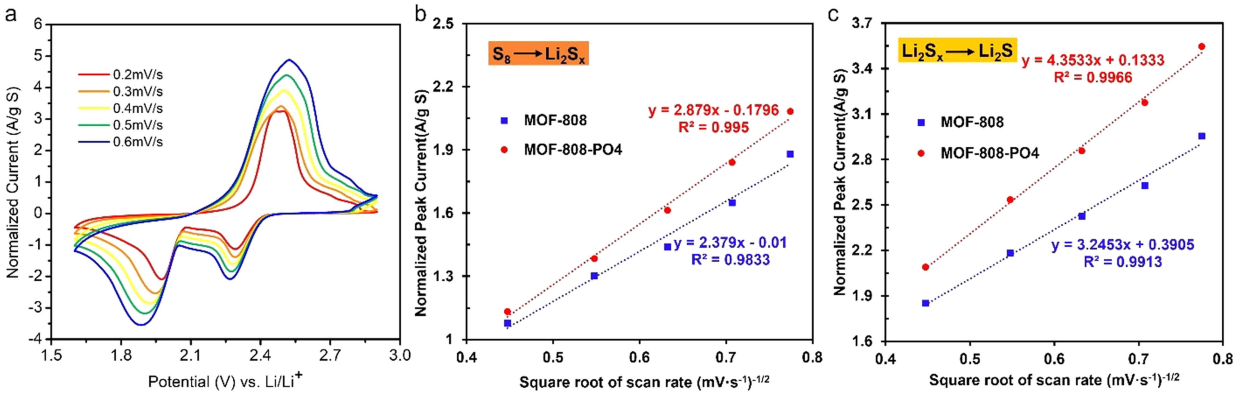

Figure 3. a) Cyclic voltammograms of coin cells constructed with MOF-808-PO4/S composite cathodes. The cells were cycled between 1.6 V and 2.9 V (vs. Li/Li^+) at various scan rates. b, c) Scan rate dependence plot. Sulfur mass-normalized peak current was plotted as a function of the square root of scan rate for the two-stage reduction of MOF/S composite cathodes.

(Figure S9a) to investigate their self-discharge behavior. Although they start at similar potentials, the MOF-808-PO4/S cell exhibits a slower rate of voltage drop and stabilization at higher OCP at the end of rest time (≈2.42 V) compared to MOF-808/S cell (≈2.38 V). Furthermore, the cells were first fully charged during the rest period prior to discharging and the ratio of 1st cycle charge capacity to discharge capacity were compared to evaluate the extent of self-discharge (Figure S9b). MOF-808-PO4/S cells demonstrate little to no capacity loss (0 to 1%), while MOF-808/S cells show drastic loss as high as 6.5%. Such results show MOF-808-PO4 can effectively slow down self-discharge rate.

The impact of phosphate functionalization on cycling performance was then investigated. Cells with MOF-808-PO4/S and MOF-808/S composite cathodes were cycled at various charge/discharge rates (C-rates, 1C is a full charge in 1 h) to examine their long-term cyclability and rate capability. For long-term cycling at 0.1C for 20 cycles and then 0.2C for 100 cycles, MOF-808-PO4/S cells demonstrate remarkably higher initial capacity, reaching an average of 1081 mAh g^{-1} compared to 854 mAh g^{-1} for the parent MOF cathodes (Figure 4a). Previously, we have shown increased local lithium ion concentration can lead to capacity improvement.[19,53] In this work, atomic absorption spectroscopy (AAS) showed a low Li content of 0.007% by mass in MOF-808-PO4, ruling out the possibility that the capacity enhancement is caused by the presence of Li ions during synthesis. Thus, the boost in maximum capacity validates the hypothesis that incorporation of phosphate groups facilitates sulfur redox.

Additionally, MOF-808-PO4/S cells show improved capacity retention, holding 84% of the initial capacity with an average of 907 mAh g^{-1} at the end of 20th cycle at 0.1C (Table S2). In contrast, MOF-808/S cells only maintain 77% of their initial capacity with an average of 247 mAh g^{-1} less capacity than

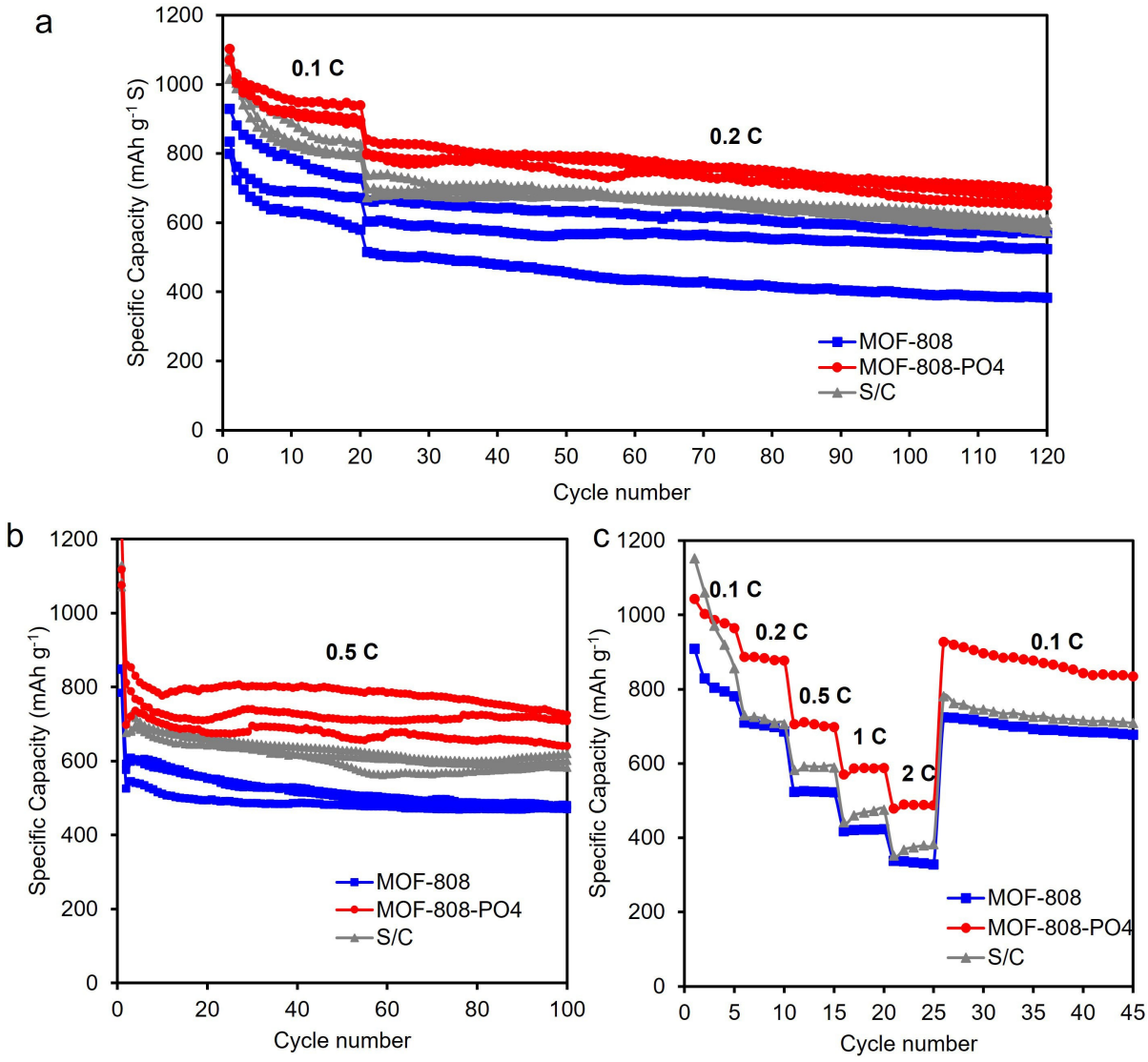

Figure 4. Cycling results of MOF-808/S, MOF-808-PO4/S and S/C cells at a) 0.1C×20 cycles, 0.2C×100 cycles, b) 0.1C×1 cycle, 0.5C×100 cycles, c) 0.1C×5 cycles, 0.2C×5 cycles, 0.5C×5 cycles, 1C×5 cycles, 2C×5 cycles, and 0.1C×20 cycles. Triplicate cells are shown to demonstrate reproducibility in (a) and (b).

MOF-808-PO4/S cells. We observe the same trend when the cells were subsequently cycled at 0.2 C for 100 cycles, where MOF-808-PO4/S cells continues to have higher capacity and retention. The improvement in capacity retention using MOF-808-PO4 suggests inhibited polysulfide dissolution is a result of the strong affinity between the phosphate groups and polysulfide species. MOF-808-PO4/S cathodes also demonstrate higher capacity retention than 45% sulfur/carbon (S/C) composite cathodes (76% of initial capacity at the end of 20th cycle), illustrating the critical role of porous hosts for polysulfide encapsulation. We next probe the impact of phosphate incorporation on charge transfer by analyzing the cycling behavior at higher C-rates. When cycled at 0.5 C, MOF-808-PO4/S cells display significantly higher specific capacity than MOF-808/S cathodes, delivering an average of 689 mAh g^{-1} and 476 mAh g^{-1} after 100 cycles, respectively (Figure 4b).

Fast charging/discharging is regarded as a critical requirement for widespread utilization in electronic devices and electric vehicles. To this end, we investigated their rate capability by cycling the cells at various C rates. MOF-808-PO4/S cells demonstrate the highest capacity in comparison with MOF-808/S and S/C cells, delivering (964, 877, 698, 588, and 488) mAh g^{-1}for the last cycle at 0.1 C, 0.2 C, 0.5 C, 1 C and 2 C (Figure 4c). The capacity boost is ascribed to enhanced sulfur utilization and charge transfer efficiency of MOF-808-PO4. In addition, MOF-808-PO4 presents the best capacity retention at all rates and high capacity recovery when cycled back to 0.1 C from 2 C (Figure S10), recovering 88% of the initial capacity. Such results suggest the phosphate moiety can effectively diminish active material loss caused by shuttle effect, even at high C rates.

To reveal the charge transfer kinetics, electrochemical impedance spectroscopy (EIS) was performed on cells after cycling to a fully discharged state (Figure 5a). An equivalent circuit of R_1-R_2//CPE$_1$-R_3(W_1)//CPE$_2$ was used to model the Nyquist plot, where R_1 is the electrolyte resistance, R_2 is the resistance from the insulating species deposited on both electrodes, R_3 is the charge transfer resistance, and the W_1 is the Warburg element.[54] MOF-808-PO4/S cell shows less electrode surface resistance compared to MOF-808/S cell, suggesting phosphate addition inhibits electrode passivation by mitigating polysulfide leaching from the cathode (Table S3). Moreover, we observed lower charge transfer resistance in MOF-808-PO4/S cell, further signifying the critical role of phosphate in facilitating fast redox kinetics.

Galvanostatic charge-discharge profiles were closely examined at different C rates (Figure S11). MOF-808/S and MOF-808-PO4/S cathodes both show a typical two-plateau discharge profile, corresponding to the two stages of sulfur reduction (sulfur to long-chain polysulfides for the upper plateau and long-chain polysulfides to insoluble Li_2S_2/Li_2S for the lower plateau). The similar characteristics of profiles suggest phosphate functionalization does not change the charging/discharging mechanism. Interestingly, MOF-808-PO4/S displays more pronounced second plateau and less sloped curves compared to MOF-808/S at higher C rates. The voltage difference (ΔV) between charge and discharge curve can provide insights into polysulfide equilibrium during the cycling process. We observe the overpotentials increase with faster charge/discharge rates in both cells, while MOF-808-PO4/S demonstrates smaller ΔV at 60% state of discharge than MOF-808/S at all C-rates (Figure 5b, Figure S12). Moreover, ΔV difference between the two cathodes keeps growing as C-rate increases (Figure 5c), reaching more than 100 mV at 2 C. Our findings illustrate lower potential polarization and enhanced polysulfide equilibria in MOF-808-PO4/S, especially for fast charge/discharge.

High energy density is a crucial criterion for next-generation Li–S batteries, which requires high mass loadings of active material and high areal capacity.[55–58] However, there is a trade-off between cycling performance and sulfur loading. Currently, most batteries with high specific capacity use relatively low sulfur loadings (usually <2 mg cm^{-2}).[59,60] We thus investigated the cycling performance of MOF/S composite cathodes at various sulfur loadings. When increasing the sulfur mass loading to 3 mg (areal loading $\approx$2.4 mg cm^{-2}) per cathode, we noticed

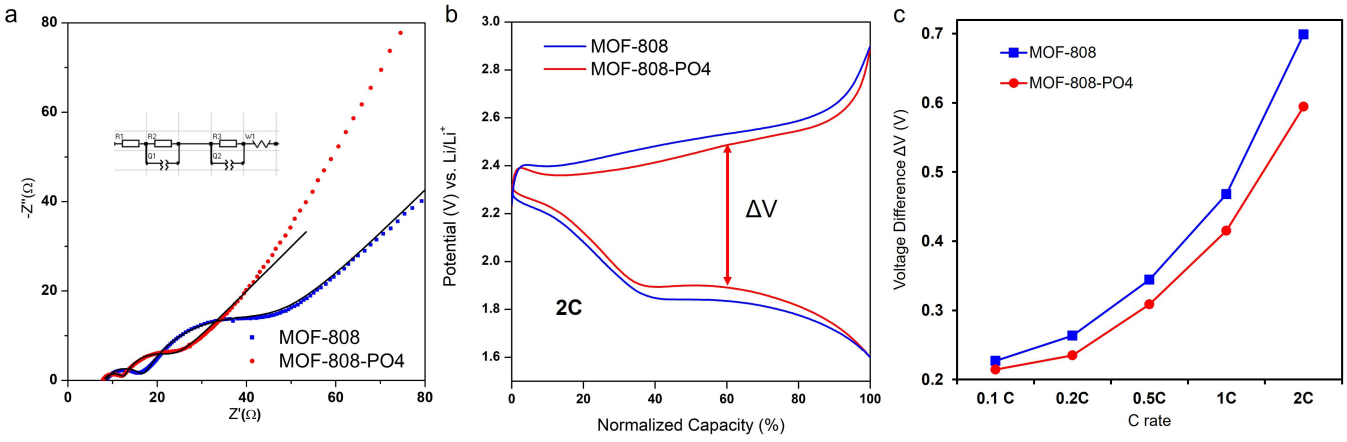

Figure 5. a) EIS and fitting curves (black line) collected on coin cells after cycling to a fully discharged state. The model circuit is shown in the inset. b) Normalized galvanostatic profiles of MOF-808/S and MOF-808-PO4/S cells at 2 C. c) Voltage differences (ΔV) at various C rates.

significant capacity differences between MOF-808-PO4/S and MOF-808/S at 1×0.1 C followed by 100 x 0.5 C (Figure 6a). The large capacity boost at all sulfur loadings tested (Figure 6b) demonstrates the excellent sulfur utilization of MOF-808-PO4. Furthermore, MOF-808-PO4 exhibits advanced rate capability compared to pristine MOF (Figure S13) at ≈2.4 mg cm^{-2} sulfur loading, illustrating its potentials towards practical high loading batteries.

Conclusion

In summary, we have developed phosphate-functionalized MOF-808 using a facile post-synthetic ligand exchange method. The phosphate interaction with the framework was characterized by IR spectroscopy, NMR spectroscopy, and X-ray pair distribution functions. MOF-808-PO4/S composite electrodes present significant capacity boost and less capacity decay compared to MOF-808/S electrodes, confirming the unique role of the framework in increasing sulfur utilization and suppressing the shuttle effect. The improved ion diffusion and charge transfer kinetics of MOF-808-PO4/S cells also benefit fast charge/discharge cycling, leading to advanced rate performance. With their enhanced sulfur utilization and capacity retention, MOF-808-PO4 was shown to improve the cyclability of Li–S batteries with high sulfur loading. Our work provides a versatile chemical platform for designing tailored materials for applications in energy storage devices.

Experimental Section

Chemicals and instrumentation

Any mention of commercial products is for informational purposes only and does not imply recommendation or endorsement by NIST. Zirconyl chloride octahydrate ($ZrOCl_2 \cdot 8H_2O$, 98%, Alfa Aesar), 1,3,5-benzenetricarboxylic acid (H_3BTC, >98%, TCI), lithium phosphate (Li_3PO_4, Acros Organics), formic acid (97%, Acros Organics), *N, N*-dimethylformamide (DMF, Sigma-Aldrich), and acetone (Fisher) were used as received without further purification.

MOF-808 and MOF-808-PO4 samples were analyzed using powder X-ray diffraction (PXRD, Bruker D8 Focus diffractometer, Cu Kα, LynxEye detector) and Fourier transform infrared spectroscopy (FTIR, ThermoScientific Nicolet iS50 FTIR). Nitrogen adsorption isotherms were collected on samples using Micromeritics ASAP 2020. Liquid-phase phosphorus nuclear magnetic resonance (^{31}P NMR) spectra were collected with a Bruker Avance II 400 MHz Spectrometer. Solid-state 31P NMR spectra were collected using a Bruker Ascend 500 MHz Spectrometer. Thermogravimetric analysis (TGA) was conducted using a TA Instruments SDT Q600 under flowing Ar at a heating rate of 5.0 °C min^{-1}. Elemental analysis by inductively coupled plasma optical emission spectroscopy (ICP-OES) was performed by Robertson Microlit Laboratories and used to quantify the P and Zr mass % in MOF-808-PO4. UV-Vis absorption spectra were collected with an Agilent Technologies Cary 60. Atomic absorption spectroscopy (AAS) was obtained using an Agilent 200 Series AA system and Agilent lithium single element hollow cathode lamp. Samples were prepared for AAS by completely dissolving approximately 11 mg of MOF powder in concentrated sulfuric acid and then diluting with deionized water. Calibration curves were prepared using standard solutions of $LiNO_3$.

Syntheses

Synthesis of MOF-808: MOF-808 was prepared using previously reported procedures.[41] H_3BTC (0.105 g, 0.5 mmol) and $ZrOCl_2 \cdot 8H_2O$ (0.485 g, 1.5 mmol) was dissolved in a 1:1 volumetric ratio of DMF/formic acid (22.5 mL/22.5 mL). The solution was then heated at 130 °C in an oven for 2 d. A white precipitate was collected by centrifugation and filtration. As-synthesized MOF-808 powder was then washed with DMF (20 mL, replaced 3 times per day) for 3 d, then with DI water (3×20 mL) for 3 d, and finally with acetone (3×20 mL) for 3 d. The product was then dried and stored in a desiccator until further use.

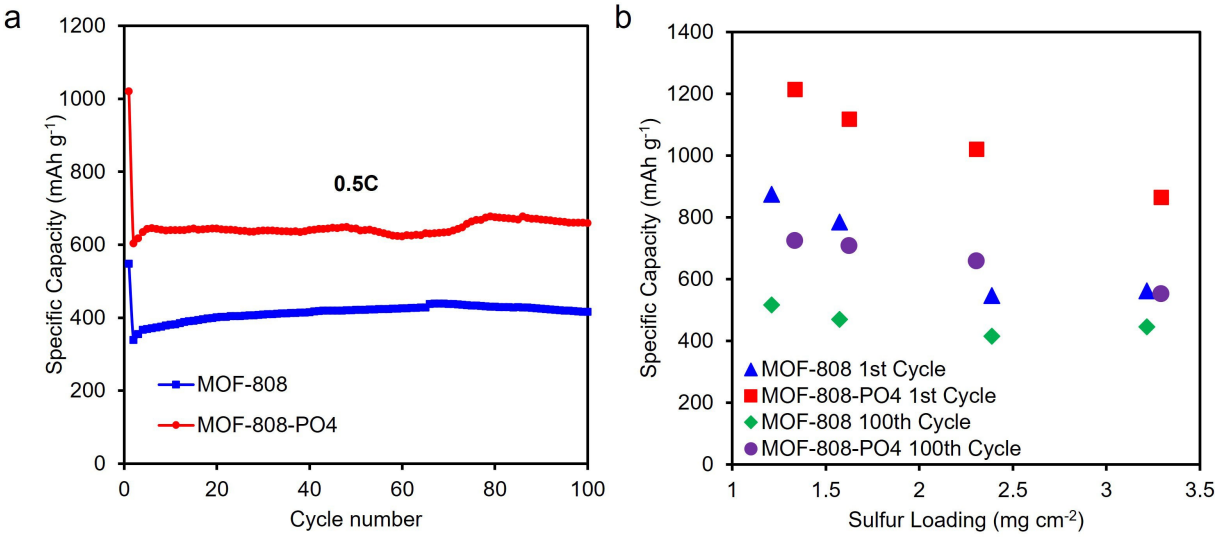

Figure 6. a) Cycling performance of cells with ≈2.4 mg cm^{-2} sulfur loading at 0.5 C (0.1 C×1 cycle, 0.5 C×100 cycles), and b) comparison of initial capacity at 0.1 C and capacity after 100 cycles at 0.5 C for various sulfur loadings.

Synthesis of MOF-808-PO4: MOF-808 was functionalized with phosphate groups using slightly modified procedures.[39,42] Li_3PO_4 (≈78 mg, 0.67 mmol) was fully dissolved in formic acid/DI water solution (little amount of formic acid was added to help dissolve) before 150 mg MOF-808 was added to the solution. After soaking at room temperature for 1 d with occasional stirring, the precursor solution was decanted. The remaining solid was further washed with DI water (3×20 mL) over 3 d, then with acetone (3×20 mL) over 3 d. Resulting phosphate incorporated MOF-808 powder were collected by centrifugation and dried for further characterization.

Synthesis of lithium polysulfides: Lithium polysulfide solutions were prepared by mixing Li_2S and S (stoichiometric ratio of 1:5 for a nominal solution of Li_2S_6) in a mixed solution of 1,2-dimethoxyethane (DME, 99+%, Alfa Aesar) and 1,3-dioxolane (DOL, 99.5%, Acros Organics) (1:1, volumetric ratio) and stirred until all solids are dissolved (between 2 to 7 d, depending on concentration).[50] The resulting solution was a dark orange color. The concentration of lithium polysulfides used in UV-Vis absorption studies is 0.04 mM.

Cathode and coin cell preparation

Both MOF-808 and MOF-808-PO4 powders were activated at 150 °C for 3 to 4 h under vacuum to remove the solvent residuals in the pores. The powders were then ground with a mortar and pestle before using as cathode additive. The cathode solid mixture was composed of 30% MOF, 45% S (Sigma-Aldrich), 15% Super-P carbon (99+%, Alfa Aesar), and 10% poly(vinylidene fluoride) (PVDF, Alfa Aesar) by mass. After MOF and sulfur were blended, PVDF, Super-P carbon, and a small stainless-steel ball were added to the mixture and the solids were vortexed for 5 min. N-methyl-2-pyrrolidinone (NMP, Oakwood Chemical) was then added to the solid mixture to form the cathode slurry. To ensure the uniformity, the slurry was thoroughly mixed in the vortex mixer for at least 30 min. Once homogenized, the slurry was cast onto pre-weighed 12.7 mm carbon paper disks (5% by mass wet-proofing, Fuel Cell Store) and dried overnight in an 80 °C oven. Upon drying, the 12.7 mm cathodes were weighed again to determine the sulfur loading and stored in an Ar-filled glovebox for use. For sulfur/carbon control cathodes (S/C), the slurry composition by mass is 45% S, 45% Super-P carbon and 10% PVDF.

CR 2032-type coin cells were assembled in an Ar-filled glovebox using a pre-weighed cathode, a polished metallic Li anode, two Celgard separators, two stainless steel spacers and a spring. The stainless steel coin cell parts were obtained from TOB New Energy. The electrolyte was composed of 1.0 mol L^{-1} bis-(trifluoromethanesulfonyl)imide lithium (LiTFSI, >99%, Acros Organics) in 1:1 DOL:DME with an added 2% by mass lithium nitrate salt ($LiNO_3$, 99%, Strem Chemicals). DOL and DME were dried with sodium metal (Sigma Aldrich) and benzophenone (99%, Sigma Aldrich) and distilled prior to use. To ensure reproducibility, the amount of electrolyte added to each coin cell assembly was normalized to sulfur loading on the cathode with the ratio of 60 μL per mg S.

Electrochemical analysis

Cyclic voltammetry (CV) was performed on freshly prepared coin cells with MOF-808/S and MOF-808-PO4/S composite cathodes. They were cycled between 1.6 V to 2.9 V (vs Li/Li^+) on an Ivium-n-STAT multichannel electrochemical analyzer to examine the electrochemical property. For cycling experiments, cells were cycled galvanostatically (MNT-BA-5 V, MicroNanoTools) after resting for 8 h. For long-term cycling, cells were cycled at a C-rate of 0.1 C for the first 20 cycles, followed by 100 cycles at 0.2 C. At least three cells were tested under the same conditions for these experiments. For long-term cycling at higher C-rates, cells were cycled at 0.1 C for the first cycle before stepping to 0.5 C and 1 C. For the rate capability test, cells were cycled at the rate of 0.1 C, 0.2 C, 0.5 C, 1 C, and 2 C for 5 cycles each, followed by 20 cycles at 0.1 C. Electrochemical impedance spectra (EIS) were collected using an Ivium-n-STAT multichannel electrochemical analyzer on the cells in the discharged state after cycling and the data was processed using Iviumsoft. The spectra were modeled by an equivalent circuit of R_1-R_2//CPE_1-$R_3(W_1)$//CPE_2, where R_1 is the electrolyte resistance, R_2 is the resistance from the insulating species deposited on both electrodes, R_3 is the charge transfer resistance, and the W_1 is the Warburg element.[54]

PDF experiment and analysis methods

The PDF data collection and node structure optimization methods were reported previously as part of a prior publication and is reproduced here for clarity.[34] Total scattering of high energy X-rays (λ = 0.2113 Å, E = 58.7 keV) was collected at beamline 11-ID–B at the Advanced Photon Source at Argonne National Laboratory using a PerkinElmer amorphous Si area detector. Powders were packed in 1.2 mm diameter Kapton capillaries. CeO_2 was used as a calibration of the setup. Integration of the patterns was performed using Fit2D freeware[61] and then reduced using PDFgetX3[62] to obtain the composition-specific scattering function, S(q), and real space correlations in the form of the pair distribution function (PDF), G(r), using a qmax of 19 $Å^{-1}$. PDF data were analyzed by least squares methods using the PDFgui program.[63] In addition to fitting, qualitative analysis used pairwise contributions (Zr–O, Zr–Zr, etc.) of the MOF node, modeled with PDFgui, to identify peak assignments.

Refinement fits for distances between 1 Å and 6 Å are presented based on the optimized structure models in Figure S4a. The refinement residuals are high owing to the simplicity of the model structure (where the organic linkers are replaced by formate molecules) and the node is optimized to a single configuration of oxo/hydroxyl/aquo ligands. Removing O–C, C–C, and O–O pairs from the calculated G(r) decreases the refinement residuals considerably (Figure S4).

Supporting Information

Additional references cited within the Supporting Information.[64–67]

Acknowledgements

We thank the National Science Foundation for the CAREER Award (DMR-1945114) and a Major Research Instrumentation grant (MRI-2018176), which enabled the acquisition of a solid-state 500 MHz Nuclear Magnetic Resonance spectrometer. B. L. also thanks the William Hooper Grafflin Fellowship from the Department of Chemistry. We acknowledge Dr. Jonathan Catazaro (Dept. of Chemistry, JHU) and Qifeng Jiang (Dept. of Chemistry, JHU) for solid-state NMR assistance. We also acknowledge Prof. Tyrel McQueen (Dept. of Chemistry, JHU) and Nicholas Ng (Dept. of Chemistry, JHU) for PXRD assistance. X-ray scattering experiments were performed at beamline 11-

ID–B at the Advanced Photon Source at Argonne National Laboratory under GUP-58814. This research was performed while A.E.B. and M.M.B. were funded under the National Research Council Research Associateship Program (NRC RAP) award at the National Institute of Standards & Technology (NIST). Any mention of commercial products is for informational purposes only and does not imply recommendation or endorsement by NIST.

Conflict of Interests

The authors declare no conflict of interest.

Data Availability Statement

The data that support the findings of this study are available from the corresponding author upon reasonable request.

Keywords: porous materials · inorganic host · sulfur redox · charge transport · energy storage devices

[1] Y. Tian, G. Zeng, A. Rutt, T. Shi, H. Kim, J. Wang, J. Koettgen, Y. Sun, B. Ouyang, T. Chen, Z. Lun, Z. Rong, K. Persson, G. Ceder, *Chem. Rev.* **2021**, *121*, 1623–1669.
[2] A. Manthiram, S. H. Chung, C. Zu, *Adv. Mater.* **2015**, *27*, 1980–2006.
[3] A. Manthiram, Y. Fu, Y. S. Su, *Acc. Chem. Res.* **2013**, *46*, 1125–1134.
[4] Y. Hu, W. Chen, T. Lei, Y. Jiao, J. Huang, A. Hu, C. Gong, C. Yan, X. Wang, J. Xiong, *Adv. Energy Mater.* **2020**, *10*, 2000082.
[5] H. J. Peng, T. Z. Hou, Q. Zhang, J. Q. Huang, X. B. Cheng, M. Q. Guo, Z. Yuan, L. Y. He, F. Wei, *Adv. Mater. Interfaces* **2014**, *1*, 1400227.
[6] G. Zheng, Q. Zhang, J. J. Cha, Y. Yang, W. Li, Z. W. Seh, Y. Cui, *Nano Lett.* **2013**, *13*, 1265–1270.
[7] X. Tao, J. Wan, C. Liu, H. Wang, H. Yao, G. Zheng, Z. W. Seh, Q. Cai, W. Li, G. Zhou, C. Zu, Y. Cui, *Nat. Commun.* **2016**, *7*, 1–9.
[8] L. Ni, G. Zhao, G. Yang, G. Niu, M. Chen, G. Diao, *ACS Appl. Mater. Interfaces* **2017**, *9*, 34793–34803.
[9] Q. Pang, D. Kundu, L. F. Nazar, *Mater. Horiz.* **2016**, *3*, 130–136.
[10] L. Wang, X. He, J. Li, M. Chen, J. Gao, C. Jiang, *Electrochim. Acta* **2012**, *72*, 114–119.
[11] L. Xiao, Y. Cao, J. Xiao, B. Schwenzer, M. H. Engelhard, L. V. Saraf, Z. Nie, G. J. Exarhos, J. Liu, *Adv. Mater.* **2012**, *24*, 1176–1181.
[12] R. Zhao, Z. Liang, R. Zou, Q. Xu, *Joule* **2018**, *2*, 2235–2259.
[13] A. E. Baumann, D. A. Burns, B. Liu, V. S. Thoi, *Commun. Chem.* **2019**, *2*, 1–14.
[14] M. Ko, L. Mendecki, A. M. Eagleton, C. G. Durbin, R. M. Stolz, Z. Meng, K. A. Mirica, *J. Am. Chem. Soc.* **2020**, *142*, 11717–11733.
[15] H. Zhong, M. Ghorbani-Asl, K. H. Ly, J. Zhang, J. Ge, M. Wang, Z. Liao, D. Makarov, E. Zschech, E. Brunner, I. M. Weidinger, J. Zhang, A. V. Krasheninnikov, S. Kaskel, R. Dong, X. Feng, *Nat. Commun.* **2020**, *11*, 1–10.
[16] D. Sheberla, J. C. Bachman, J. S. Elias, C. J. Sun, Y. Shao-Horn, M. Dincaˇ, *Nat. Mater.* **2016**, *16*, 220–224.
[17] S. Fischer, J. Roeser, T. C. erri Lin, R. H. DeBlock, J. Lau, B. S. Dunn, F. Hoffmann, M. Frçba, A. Thomas, H. Sarah Tolbert, S. Fischer, T. C. Lin, S. H. Tolbert, R. H. DeBlock, J. Lau, B. S. Dunn, D. Fischer, D. Roeser, A. Thomas, D. H. offmann, M. Frçba, *Angew. Chem. Int. Ed.* **2018**, *57*, 16683–16687.
[18] L. Shen, H. Bin Wu, F. Liu, J. L. Brosmer, G. Shen, X. Wang, J. I. Zink, Q. Xiao, M. Cai, G. Wang, Y. Lu, B. Dunn, L. Shen, H. B. Wu, F. Liu, G. Shen, X. Wang, Y. Lu, J. L. Brosmer, J. I. Zink, Q. Xiao, M. Cai, G. Wang, B. Dunn, *Adv. Mater.* **2018**, *30*, 1707476.
[19] A. E. Baumann, D. A. Burns, J. C. Díaz, V. S. Thoi, *ACS Appl. Mater. Interfaces* **2019**, *11*, 2159–2167.
[20] Y. Yang, Z. Wang, T. Jiang, C. Dong, Z. Mao, C. Lu, W. Sun, K. Sun, *J. Mater. Chem. A* **2018**, *6*, 13593–13598.
[21] Z. Wang, B. Wang, Y. Yang, Y. Cui, Z. Wang, B. Chen, G. Qian, *ACS Appl. Mater. Interfaces* **2015**, *7*, 20999–21004.
[22] H. Jiang, X. C. Liu, Y. Wu, Y. Shu, X. Gong, F. S. Ke, H. Deng, *Angew. Chem. Int. Ed.* **2018**, *57*, 3916–3921.
[23] J. Zhou, R. Li, X. Fan, Y. Chen, R. Han, W. Li, J. Zheng, B. Wang, X. Li, *Energy Environ. Sci.* **2014**, *7*, 2715–2724.
[24] B. Liu, V. S. Thoi, *Chem. Mater.* **2020**, *32*, 8450–8459.
[25] Y. Zheng, S. Zheng, H. Xue, H. Pang, *J. Mater. Chem. A* **2019**, *7*, 3469–3491.
[26] B. Liu, V. S. Thoi, *Chem. Commun.* **2022**, *58*, 4005–4015.
[27] G. Zhou, K. Liu, Y. Fan, M. Yuan, B. Liu, W. Liu, F. Shi, Y. Liu, W. Chen, J. Lopez, D. Zhuo, J. Zhao, Y. Tsao, X. Huang, Q. Zhang, Y. Cui, *ACS Cent. Sci.* **2018**, *4*, 260–267.
[28] T. Lei, W. Chen, Y. Hu, W. Lv, X. Lv, Y. Yan, J. Huang, Y. Jiao, J. Chu, C. Yan, C. Wu, Q. Li, W. He, J. Xiong, *Adv. Energy Mater.* **2018**, *8*, 1802441.
[29] C. Ma, Y. Feng, X. Liu, Y. Yang, L. Zhou, L. Chen, C. Yan, W. Wei, *Energy Storage Mater.* **2020**, *32*, 46–54.
[30] Y. Cui, Q. Zhang, J. Wu, X. Liang, A. P. Baker, D. Qu, H. Zhang, H. Zhang, X. Zhang, *J. Power Sources* **2018**, *378*, 40–47.
[31] Y. Liu, W. Yan, W. Zhang, W. Kong, Z. Wang, X. Hao, G. Guan, *ChemSusChem* **2019**, *12*, 5172–5182.
[32] J. Chen, H. Yang, X. Zhang, J. Lei, H. Zhang, H. Yuan, J. Yang, Y. Nuli, J. Wang, *ACS Appl. Mater. Interfaces* **2019**, *11*, 33419–33427.
[33] H. Yang, C. Guo, J. Chen, A. Naveed, J. Yang, Y. Nuli, J. Wang, *Angew. Chem. Int. Ed.* **2019**, *58*, 791–795.
[34] A. E. Baumann, X. Han, M. M. Butala, V. S. Thoi, *J. Am. Chem. Soc.* **2019**, *141*, 17891–17899.
[35] A. E. Baumann, J. R. Downing, D. A. Burns, M. C. Hersam, V. Sara Thoi, *ACS Appl. Mater. Interfaces* **2020**, *12*, 37173–37181.
[36] D. A. Burns, A. E. Baumann, K. J. Bennett, J. C. Díaz, V. S. Thoi, *ACS Appl. Mater. Interfaces* **2021**, *13*, 50862–50868.
[37] J. M. Yang, *J. Colloid Interface Sci.* **2017**, *505*, 178–185.
[38] M. Yabushita, P. Li, T. Islamoglu, H. Kobayashi, A. Fukuoka, O. K. Farha, A. Katz, *Ind. Eng. Chem. Res.* **2017**, *56*, 7141–7148.
[39] S. Wang, C. M. McGuirk, M. B. Ross, S. Wang, P. Chen, H. Xing, Y. Liu, C. A. Mirkin, *J. Am. Chem. Soc.* **2017**, *139*, 9827–9830.
[40] Y. Bai, Y. Dou, L. H. Xie, W. Rutledge, J. R. Li, H. C. Zhou, *Chem. Soc. Rev.* **2016**, *45*, 2327–2367.
[41] J. Jiang, F. Gándara, Y. B. Zhang, K. Na, O. M. Yaghi, W. G. Klemperer, *J. Am. Chem. Soc.* **2014**, *136*, 12844–12847.
[42] P. Deria, W. Bury, I. Hod, C. W. Kung, O. Karagiaridi, J. T. Hupp, O. K. Farha, *Inorg. Chem.* **2015**, *54*, 2185–2192.
[43] S. D. Jiang, Q. Z. Yao, Y. F. Ma, G. T. Zhou, S. Q. Fu, *Gondwana Res.* **2015**, *28*, 858–868.
[44] K. N. Rao, A. Sridhar, A. F. Lee, S. J. Tavener, N. A. Young, K. Wilson, *Green Chem.* **2006**, *8*, 790–797.
[45] E. Plessers, G. Fu, C. Y. X. Tan, D. E. De Vos, M. B. J. Roeffaers, *Catal.* **2016**, *6*, 104.
[46] C. Koschnick, R. Stäglich, T. Scholz, M. W. Terban, A. von Mankowski, G. Savasci, F. Binder, A. Schökel, M. Etter, J. Nuss, R. Siegel, L. S. Germann, C. Ochsenfeld, R. E. Dinnebier, J. Senker, B. V. Lotsch, *Nat. Commun.* **2021**, *12*, 1–9.
[47] H. Xu, S. Sommer, N. L. N. Broge, J. Gao, B. B. Iversen, *Chem. A Eur. J.* **2019**, *25*, 2051–2058.
[48] T. D. Bennett, T. K. Todorova, E. F. Baxter, D. G. Reid, C. Gervais, B. Bueken, B. Van De Voorde, D. De Vos, D. A. Keen, C. Mellot-Draznieks, *Phys. Chem. Chem. Phys.* **2016**, *18*, 2192–2201.
[49] M. W. Terban, S. K. Ghose, A. M. Plonka, D. Troya, P. Juhás, R. E. Dinnebier, J. J. Mahle, W. O. Gordon, A. I. Frenkel, *Commun. Chem.* **2021**, *4*, 1–10.
[50] A. Gupta, A. Bhargav, A. Manthiram, *Adv. Energy Mater.* **2019**, *9*, 1803096.
[51] A. J. Bard, L. R. Faulkner, *John Wiley & Sons, Inc.* **2001**.
[52] J. Q. Huang, T. Z. Zhuang, Q. Zhang, H. J. Peng, C. M. Chen, F. Wei, *ACS Nano* **2015**, *9*, 3002–3011.
[53] B. Liu, A. E. Baumann, V. S. Thoi, *Polyhedron* **2019**, *170*, 788–795.
[54] V. S. Kolosnitsyn, E. V. Kuzmina, E. V. Karaseva, S. E. Mochalov, *J. Power Sources* **2011**, *196*, 1478–1482.
[55] B. J. Lee, C. Zhao, J. H. Yu, T. H. Kang, H. Y. Park, J. Kang, Y. Jung, X. Liu, T. Li, W. Xu, X. B. Zuo, G. L. Xu, K. Amine, J. S. Yu, *Nat. Commun.* **2022**, *13*, 1–11.
[56] R. Liu, W. Liu, Y. Bu, W. Yang, C. Wang, C. Priest, Z. Liu, Y. Wang, J. Chen, Y. Wang, J. Cheng, X. Lin, X. Feng, G. Wu, Y. Ma, W. Huang, *ACS Nano* **2020**, *14*, 17308–17320.

[57] S. Tu, Z. Chen, B. Zhang, X. Wang, R. Zhan, C. Li, Y. Sun, *Nano Lett.* **2022**, *22*, 5982–5989.
[58] B. Wang, L. Wang, B. Zhang, S. Zeng, F. Tian, J. Dou, Y. Qian, L. Xu, *ACS Nano* **2022**, *16*, 4947–4960.
[59] M. Hagen, D. Hanselmann, K. Ahlbrecht, R. Maça, D. Gerber, J. Tübke, M. Hagen, D. Hanselmann, K. Ahlbrecht, R. Maça, D. Gerber, J. Tübke, *Adv. Energy Mater.* **2015**, *5*, 1401986.
[60] M. Zhao, B. Q. Li, X. Q. Zhang, J. Q. Huang, Q. Zhang, *ACS Cent. Sci.* **2020**, *6*, 1095–1104.
[61] A. P. Hammersley, S. O. Svensson, M. Hanfland, A. N. Fitch, D. Häusermann, *High Pressure Res.* **2006**, *14*, 235–248.
[62] P. Juhás, T. Davis, C. L. Farrow, S. J. L. Billinge, *J. Appl. Crystallogr.* **2013**, *46*, 560–566.
[63] C. L. Farrow, P. Juhas, J. W. Liu, D. Bryndin, E. S. Boin, J. Bloch, T. Proffen, S. J. L. Billinge, *J. Phys. Condens. Matter* **2007**, *19*, 335219.
[64] P. Geng, M. Du, X. Guo, H. Pang, Z. Tian, P. Braunstein, Q. Xu, *Energy Environ. Mater.* **2022**, *5*, 599–607.
[65] A. Benítez, J. Amaro-Gahete, D. Esquivel, F. J. Romero-Salguero, J. Morales, Á. Caballero, *Nanomaterials* **2020**, *10*, 10030424.
[66] D. Cai, M. Lu, L. Li, J. Cao, D. Chen, H. Tu, J. Li, W. Han, *Small* **2019**, *15*, 1902605.
[67] D. Yang, Z. Liang, P. Tang, C. Zhang, M. Tang, Q. Li, J. J. Biendicho, J. Li, M. Heggen, R. E. Dunin-Borkowski, M. Xu, J. Llorca, J. Arbiol, J. R. Morante, S.-L. Chou, A. Cabot, *Adv. Mater.* **2022**, *34*, 2108835.

Manuscript received: March 14, 2023
Accepted manuscript online: May 8, 2023
Version of record online: ■■, ■■

RESEARCH ARTICLE

Functional framework: A phosphate-functionalized metal–organic framework improves charge transport and enhances sulfur utilization as sulfur cathode additive for lithium–sulfur batteries.

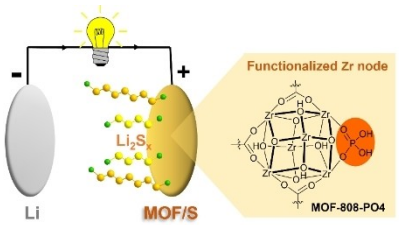

*Dr. B. Liu, Dr. A. E. Baumann, Prof. Dr. M. M. Butala, Prof. Dr. V. S. Thoi**

1 – 11

Phosphate-functionalized Zirconium Metal–Organic Frameworks for Enhancing Lithium–Sulfur Battery Cycling